Available online at www.sciencedirect.com
ScienceDirect
International Journal of Heat and Mass Transfer 51 (2008) 3207–3216
International Journal of HEAT and MASS TRANSFER
www.elsevier.com/locate/ijhmt

# Lattice Boltzmann simulation of collision dynamics of two unequal-size droplets

Bumpei Sakakibara [a], Takaji Inamuro [a,b,*]

[a] Department of Aeronautics and Astronautics, Graduate School of Engineering, Kyoto University, Kyoto 606-8501, Japan
[b] Advanced Research Institute of Fluid Science and Engineering, Graduate School of Engineering, Kyoto University, Kyoto 606-8501, Japan

Received 5 September 2007; received in revised form 6 February 2008
Available online 1 April 2008

**Abstract**

The lattice Boltzmann method for two-phase fluid flows with large density ratios is applied to the simulations of the collision dynamics of two unequal-size droplets with the diameter ratios of $\lambda = 0.5$ and 0.25 for various Weber numbers of $30 < We < 140$ and impact parameters of $0 \leqslant B \leqslant 0.75$ at Reynolds numbers of $3900 \leqslant Re \leqslant 4900$. The density ratio of the liquid to the gas is fixed at 50. Coalescence collision and two different types of separating collisions, namely reflexive and stretching separations, are simulated. The boundaries between the coalescence collision and both of the separating collisions are found and compared with available theoretical predictions. The mixing processes during separating collisions with $\lambda = 0.5$ for various Weber numbers are also simulated by tracing colored particles embedded in the droplets, and the relation between the mixing rate and the Weber number is obtained.


## 1. Introduction

The phenomena of binary droplet collision are of fundamental importance in the studies of raindrop formation, spraying processes, dispersed phase systems, and so on. Therefore, many investigations of the binary droplet collision dynamics have been performed by using experimental, numerical, and theoretical approaches [1–5]. In particular, numerical simulations are currently in progress to enhance the physical understanding of fluid dynamics inside the droplets which cannot be readily studied experimentally [6–11].

Mashayek et al. [6] studied the axisymmetric coalescence of two liquid drops using a Galerkin finite element method with the spline-flux scheme for tracking the free surface. The effects of Reynolds number, impact velocity, drop size ratio, and internal circulation on the coalescence process were investigated. Inamuro et al. [15] proposed a two-phase lattice Boltzmann method (two-phase LBM) for large density ratios and investigated binary droplet collisions with a density ratio of 50 for various Weber numbers and impact parameters [7]. In addition, the mixing processes during separating collisions were simulated for various impact parameters. Dai and Schmidt [8] investigated the effect of viscosity on the maximum deformation amplitude for a head-on collision of two equal-size droplets using a moving-mesh finite-volume method. Pan and Suga [9] studied the process of the collision of two liquid droplets by solving the incompressible Navier–Stokes equations coupled with the convective equation of the level set function. Premnath and Abraham [10] used a multiple-relaxation-time lattice Boltzmann method for simulating binary droplet collisions with low density ratios and investigated the effects of the Weber number and the Ohnesorge number on the characteristics of collisions. Meleán and Sigalotti [11] investigated the coalescence of two equal-sized

* Corresponding author. Address: Department of Aeronautics and Astronautics, Graduate School of Engineering, Kyoto University, Kyoto 606-8501, Japan. Tel.: +81 75 753 5791; fax: +81 75 753 4947.
*E-mail address:* inamuro@kuaero.kyoto-u.ac.jp (T. Inamuro).

0017-9310/$ - see front matter © 2008 Elsevier Ltd. All rights reserved.
doi:10.1016/j.ijheatmasstransfer.2008.02.004

**Nomenclature**

| | |
|---|---|
| $a$ | free parameter determining $\phi$ |
| $b$ | free parameter determining $\phi$ |
| $B$ | impact parameter, $2X/(D_\mathrm{l}+D_\mathrm{s})$ |
| $c$ | characteristic particle speed |
| $\boldsymbol{c}_i$ | particle velocity |
| $D_\mathrm{l}$ | diameter of larger droplet |
| $D_\mathrm{s}$ | diameter of smaller droplet |
| $E_i$ | constants in equilibrium distribution functions |
| $F_i$ | constants in equilibrium distribution functions |
| $f_i$ | particle velocity distribution function for an order parameter |
| $f_i^{\mathrm{eq}}$ | equilibrium distribution function for $f_i$ |
| $g_i$ | particle velocity distribution function for a multicomponent fluid |
| $g_i^{\mathrm{eq}}$ | equilibrium distribution function for $g_i$ |
| $h_i$ | particle velocity distribution function for pressure |
| $H_i$ | constants in equilibrium distribution functions |
| $L$ | characteristic length |
| $p$ | pressure |
| $p_0$ | function determining $\phi$ |
| $Re$ | Reynolds number, $\rho_\mathrm{L}D_\mathrm{l}V/\mu_\mathrm{L}$ |
| $Sh$ | Strouhal number, $U/c$ |
| $t$ | time |
| $t_0$ | characteristic time scale, $L/U$ |
| $t^*$ | characteristic time after release, $2tV/(D_\mathrm{l}+D_\mathrm{s})$ |
| $T$ | free parameter determining $\phi$ |
| $\boldsymbol{u}$ | current velocity of a multicomponent fluid |
| $\boldsymbol{u}^*$ | predicted velocity of a multicomponent fluid |
| $U$ | characteristic flow speed |
| $V$ | relative velocity of binary collision |
| $We$ | Weber number, $\rho_\mathrm{L}D_\mathrm{s}V^2/\sigma$ |
| $\boldsymbol{x}$ | Cartesian coordinates, $(x,y,z)$ |
| $X$ | distance from the center of one droplet to the relative velocity vector on the center of the other droplet |

*Greek symbols*

| | |
|---|---|
| $\delta_{\alpha\beta}$ | Kronecher delta |
| $\Delta x$ | lattice spacing |
| $\Delta t$ | time step |
| $\kappa_f$ | constant parameter determining the width of interface |
| $\kappa_g$ | constant parameter determining the strength of surface tension |
| $\lambda$ | diameter ratio, $D_\mathrm{s}/D_\mathrm{l}$ |
| $\mu$ | viscosity |
| $\rho$ | density |
| $\rho_0$ | reference density |
| $\sigma$ | surface tension |
| $\tau_f$ | relaxation time for $f_i$ |
| $\tau_g$ | relaxation time for $g_i$ |
| $\tau_h$ | relaxation time for $h_i$ |
| $\phi$ | order parameter representing an interface |

*Subscripts*

| | |
|---|---|
| G | gas phase |
| L | liquid phase |
| $\alpha$ | Cartesian coordinates |
| $\beta$ | Cartesian coordinates |
| $\gamma$ | Cartesian coordinates |

infinitely long cylinders using the method of smoothed particle hydrodynamics.

The above-mentioned researches by experimental, numerical, and theoretical approaches were focused mainly on the collisions of two equal-size droplets, and the collision dynamics of two unequal-size droplets has been little understood, although it is very important for practical problems. In particular, the collision of two unequal-size droplets with the diameter ratio less than 0.5 has not been investigated so much. Experimental data for the diameter ratio less than 0.5 are little, and also the theoretical predictions of reflexive and stretching separations by Ashgriz and Poo [2] and by Brazier-Smith et al. [16] become unclear as the diameter ratio is small.

The aim of the present paper is to apply the two-phase LBM [7,15,17] to simulations of the collision dynamics of two unequal-size droplets for various Weber numbers and impact parameters. The calculated results are classified into coalescence collision and two different types of separating collisions, namely reflexive and stretching separations, and the boundaries of three types of collisions are compared with available theoretical predictions. The mixing processes during separating collisions for various Weber numbers are also simulated by tracing colored particles embedded in the droplets.

## 2. Numerical method

Non-dimensional variables, which are defined by using a characteristic length $L$, a characteristic particle speed $c$, a characteristic time scale $t_0 = L/U$, where $U$ is a characteristic flow speed, and a reference density $\rho_0$, are used as in [13]. In the LBM, a modeled fluid, composed of identical particles whose velocities are restricted to a finite set of $N$ vectors $\boldsymbol{c}_i$ $(i = 1, 2, \ldots, N)$, is considered. The 15-velocity model $(N = 15)$ is used in the present paper. The velocity vectors of this model are given by

$$[\boldsymbol{c}_1,\boldsymbol{c}_2,\boldsymbol{c}_3,\boldsymbol{c}_4,\boldsymbol{c}_5,\boldsymbol{c}_6,\boldsymbol{c}_7,\boldsymbol{c}_8,\boldsymbol{c}_9,\boldsymbol{c}_{10},\boldsymbol{c}_{11},\boldsymbol{c}_{12},\boldsymbol{c}_{13},\boldsymbol{c}_{14},\boldsymbol{c}_{15}] = \begin{bmatrix} 0 & 1 & 0 & 0 & -1 & 0 & 0 & 1 & -1 & 1 & 1 & -1 & 1 & -1 & -1 \\ 0 & 0 & 1 & 0 & 0 & -1 & 0 & 1 & 1 & -1 & 1 & -1 & -1 & 1 & -1 \\ 0 & 0 & 0 & 1 & 0 & 0 & -1 & 1 & 1 & 1 & -1 & -1 & -1 & -1 & 1 \end{bmatrix}. \tag{1}$$

The physical space is divided into a cubic lattice, and the evolution of particle population at each lattice site is computed. Two particle velocity distribution functions, $f_i$ and $g_i$, are used. The function $f_i$ is used for the calculation of an order parameter which represents the difference between two phases, and the function $g_i$ is used for the calculation of a predicted velocity of the two-phase fluid without a pressure gradient. The evolution of the particle distribution functions $f_i(\boldsymbol{x},t)$ and $g_i(\boldsymbol{x},t)$ with velocity $\boldsymbol{c}_i$ at the point $\boldsymbol{x}$ and at time $t$ is computed by the following equations:

$$f_i(\boldsymbol{x}+\boldsymbol{c}_i\Delta x, t+\Delta t) = f_i(\boldsymbol{x},t) - \frac{1}{\tau_f}[f_i(\boldsymbol{x},t) - f_i^{\mathrm{eq}}(\boldsymbol{x},t)], \tag{2}$$

$$g_i(\boldsymbol{x}+\boldsymbol{c}_i\Delta x, t+\Delta t) = g_i(\boldsymbol{x},t) - \frac{1}{\tau_g}[g_i(\boldsymbol{x},t) - g_i^{\mathrm{eq}}(\boldsymbol{x},t)] + 3E_i c_{i\alpha}\frac{1}{\rho}\left[\frac{\partial}{\partial x_\beta}\mu\left(\frac{\partial u_\beta}{\partial x_\alpha}+\frac{\partial u_\alpha}{\partial x_\beta}\right)\right]\Delta x, \tag{3}$$

where $f_i^{\mathrm{eq}}$ and $g_i^{\mathrm{eq}}$ are equilibrium distribution functions, $\tau_f$ and $\tau_g$ are dimensionless single relaxation times, $\Delta x$ is a spacing of the cubic lattice, $\Delta t$ is a time step during which the particles travel the lattice spacing, and the other variables, $\rho$, $\mu$ and $\boldsymbol{u}$, and constants $E_i$ are defined below.

The order parameter $\phi$ representing the difference between two phases and the predicted velocity $\boldsymbol{u}^*$ of the two-phase fluid are defined in terms of the two particle velocity distribution functions as follows:

$$\phi = \sum_{i=1}^{15} f_i, \tag{4}$$

$$\boldsymbol{u}^* = \sum_{i=1}^{15} \boldsymbol{c}_i g_i. \tag{5}$$

The equilibrium distribution functions in Eqs. (2) and (3) are given by

$$f_i^{\mathrm{eq}} = H_i\phi + F_i\left[p_0 - \kappa_f\phi\frac{\partial^2\phi}{\partial x_\alpha^2} - \frac{\kappa_f}{6}\left(\frac{\partial\phi}{\partial x_\alpha}\right)^2\right] + 3E_i\phi c_{i\alpha}u_\alpha + E_i\kappa_f G_{\alpha\beta}(\phi)c_{i\alpha}c_{i\beta}, \tag{6}$$

$$g_i^{\mathrm{eq}} = E_i\left[1 + 3c_{i\alpha}u_\alpha - \frac{3}{2}u_\alpha u_\alpha + \frac{9}{2}c_{i\alpha}c_{i\beta}u_\alpha u_\beta + \frac{3}{2}\left(\tau_g - \frac{1}{2}\right)\Delta x\left(\frac{\partial u_\beta}{\partial x_\alpha}+\frac{\partial u_\alpha}{\partial x_\beta}\right)c_{i\alpha}c_{i\beta}\right] + E_i\frac{\kappa_g}{\rho}G_{\alpha\beta}(\rho)c_{i\alpha}c_{i\beta} - \frac{2}{3}F_i\frac{\kappa_g}{\rho}\left(\frac{\partial\rho}{\partial x_\alpha}\right)^2, \tag{7}$$

where

$$\begin{aligned} &E_1 = 2/9, \quad E_2 = E_3 = E_4 = \cdots = E_7 = 1/9, \\ &E_8 = E_9 = E_{10} = \cdots = E_{15} = 1/72, \\ &H_1 = 1, \quad H_2 = H_3 = H_4 = \cdots = H_{15} = 0, \\ &F_1 = -7/3, \quad F_i = 3E_i \quad (i = 2,3,4,\ldots,15), \end{aligned} \tag{8}$$

and

$$G_{\alpha\beta}(\phi) = \frac{9}{2}\frac{\partial\phi}{\partial x_\alpha}\frac{\partial\phi}{\partial x_\beta} - \frac{3}{2}\frac{\partial\phi}{\partial x_\gamma}\frac{\partial\phi}{\partial x_\gamma}\delta_{\alpha\beta}, \tag{9}$$

with $\alpha,\beta,\gamma = x,y,z$ (subscripts $\alpha$, $\beta$, and $\gamma$ represent Cartesian coordinates and the summation convention is used). In the above equations, $\delta_{\alpha\beta}$ is the Kronecker delta, $\kappa_f$ is a constant parameter determining the width of the interface, and $\kappa_g$ is a constant parameter determining the strength of the surface tension. In Eq. (6), $p_0$ is given by

$$p_0 = \phi T\frac{1}{1-b\phi} - a\phi^2, \tag{10}$$

where $a$, $b$, and $T$ are free parameters determining the maximum and minimum values of the order parameter $\phi$. It is noted that $f_i^{\mathrm{eq}}$ is the same as that of the Swift et al. model [12]. The following finite-difference approximations are used to calculate the derivatives in Eqs. (6), (7), and (9):

$$\frac{\partial\psi}{\partial x_\alpha} \approx \frac{1}{10\Delta x}\sum_{i=2}^{15} c_{i\alpha}\psi(\boldsymbol{x}+\boldsymbol{c}_i\Delta x), \tag{11}$$

$$\nabla^2\psi \approx \frac{1}{5(\Delta x)^2}\left[\sum_{i=2}^{15}\psi(\boldsymbol{x}+\boldsymbol{c}_i\Delta x) - 14\psi(\boldsymbol{x})\right]. \tag{12}$$

The density in the interface is obtained by using the cut-off values of the order parameter, $\phi_{\mathrm{L}}^*$ and $\phi^*{}_{\mathrm{G}}$, for the liquid and gas phases with the following relation:

$$\rho = \begin{cases} \rho_{\mathrm{G}}, & \phi < \phi_{\mathrm{G}}^*, \\ \frac{\Delta\rho}{2}\left[\sin\left(\frac{\phi-\overline{\phi^*}}{\Delta\phi^*}\pi\right)+1\right] + \rho_{\mathrm{G}}, & \phi_{\mathrm{G}}^* \leqslant \phi \leqslant \phi_{\mathrm{L}}^*, \\ \rho_{\mathrm{L}}, & \phi > \phi_{\mathrm{L}}^*, \end{cases} \tag{13}$$

where $\rho_{\mathrm{G}}$ and $\rho_{\mathrm{L}}$ are the density of gas and liquid phase, respectively, $\Delta\rho = \rho_{\mathrm{L}} - \rho_{\mathrm{G}}$, $\Delta\phi^* = \phi_{\mathrm{L}}^* - \phi_{\mathrm{G}}^*$, and $\overline{\phi^*} = (\phi_{\mathrm{L}}^* + \phi_{\mathrm{G}}^*)/2$. The viscosity $\mu$ in the interface is obtained by

$$\mu = \frac{\rho-\rho_{\mathrm{G}}}{\rho_{\mathrm{L}}-\rho_{\mathrm{G}}}(\mu_{\mathrm{L}} - \mu_{\mathrm{G}}) + \mu_{\mathrm{G}}, \tag{14}$$

where $\mu_{\mathrm{G}}$ and $\mu_{\mathrm{L}}$ are the viscosity of gas and liquid phase, respectively.

The surface tension $\sigma$ is given by

$$\sigma = \kappa_g \int_{-\infty}^{\infty} \left(\frac{\partial \rho}{\partial \xi}\right)^2 \mathrm{d}\xi, \tag{15}$$

with $\xi$ being the coordinate normal to the interface [14].

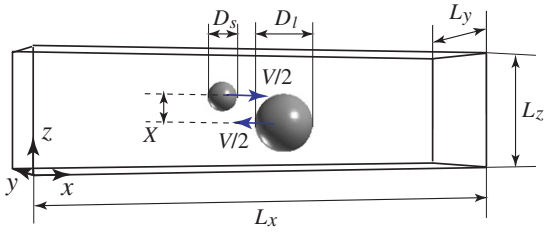


Fig. 1. Computational domain and two unequal-size droplets.

Since $\boldsymbol{u}^*$ is not divergence free ($\nabla \cdot \boldsymbol{u}^* \neq 0$), the correction of $\boldsymbol{u}^*$ is required. The current velocity $\boldsymbol{u}$ which satisfies the continuity equation ($\nabla \cdot \boldsymbol{u} = 0$) can be obtained by using the following equations:

$$Sh\frac{\boldsymbol{u} - \boldsymbol{u}^*}{\Delta t} = -\frac{\nabla p}{\rho}, \tag{16}$$

$$\nabla \cdot \left(\frac{\nabla p}{\rho}\right) = Sh\frac{\nabla \cdot \boldsymbol{u}^*}{\Delta t}, \tag{17}$$

where $Sh = U/c$ is the Strouhal number and $p$ is the pressure. The Poisson equation (17) can be solved by various methods. In the present paper, we solve Eq. (17) in the framework of LBM. Namely, the following evolution equation of the velocity distribution function $h_i$ is used for the calculation of the pressure $p$:

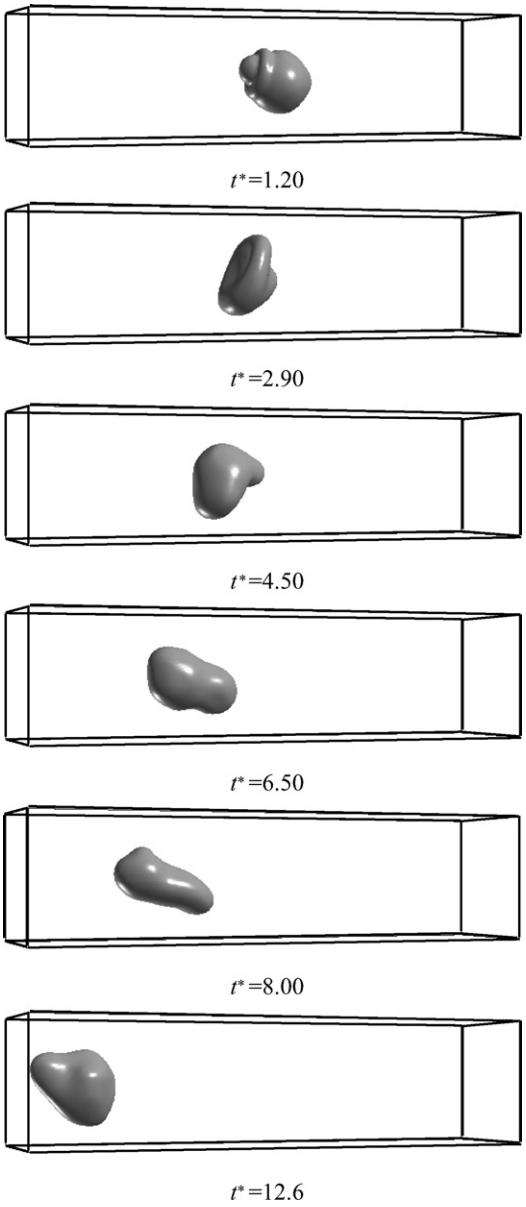


Fig. 2. Time evolution of droplet shape for $\lambda = 0.5$, $We = 30.8$, and $B = 0.25$ [$t^* = 2tV/(D_l + D_s)$].

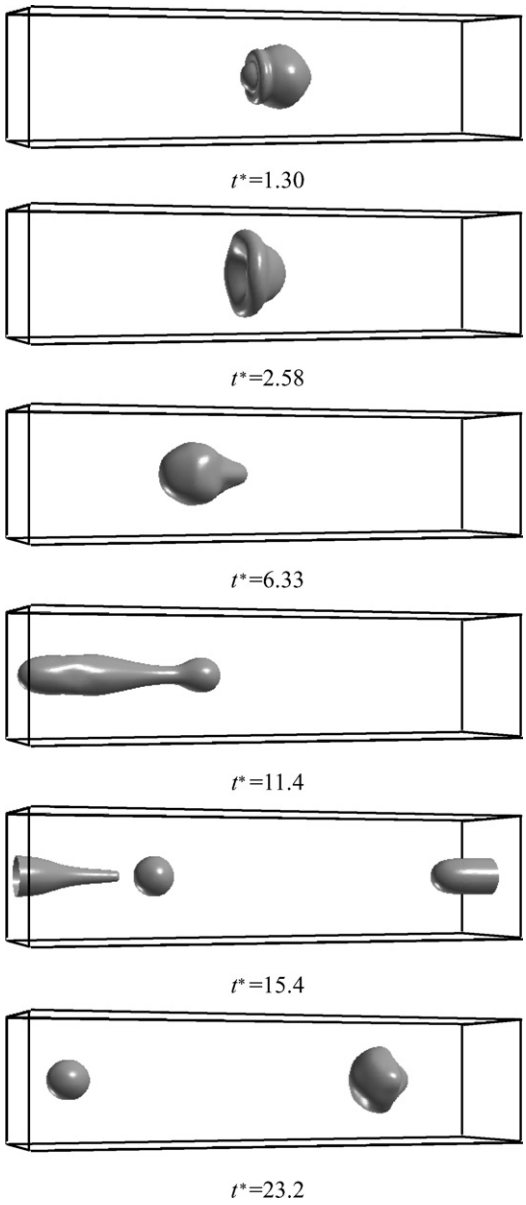


Fig. 3. Time evolution of droplet shape for $\lambda = 0.5$, $We = 51.3$, and $B = 0$ [$t^* = 2tV/(D_l + D_s)$].

$$h_i^{n+1}(\boldsymbol{x}+\boldsymbol{c}_i\Delta x) = h_i^n(\boldsymbol{x}) - \frac{1}{\tau_h}\left[h_i^n(\boldsymbol{x}) - E_i p^n(\boldsymbol{x})\right] - \frac{1}{3}E_i\frac{\partial u_\alpha^*}{\partial x_\alpha}\Delta x, \tag{18}$$

where $n$ is the number of iterations and the relaxation time $\tau_h$ is given by

$$\tau_h = \frac{1}{\rho} + \frac{1}{2}. \tag{19}$$

The pressure is obtained by

$$p = \sum_{i=1}^{15} h_i. \tag{20}$$

The iteration of Eq. (18) is repeated until $|\,p^{n+1} - p^n\,|/\rho < 10^{-5}$ is satisfied in the whole domain.

Applying the asymptotic theory [18] to Eqs. (2), (3) and (18), we find that the asymptotic expansions of macroscopic variables, $\phi, \rho, \boldsymbol{u}$, and $p$, satisfy the phase-field advection–diffusion equation (the Cahn–Hilliard equation with advection) for $\phi$, the continuity equation, and the Navier–Stokes equations for incompressible two-phase fluid with relative errors of $O[(\Delta x)^2]$ [15].

In preliminary calculations, it is found that using the present method we can simulate two-phase flows with the density ratio up to 1000, but the iteration of Eq. (18) needs more computation time as the increase of the density ratio. In the following calculations, therefore, we use the same density ratio of $\rho_L/\rho_G = 50$ as the previous paper [7] which is nearly the ratio of injected fuel to compressed oxidizer in diesel engines.

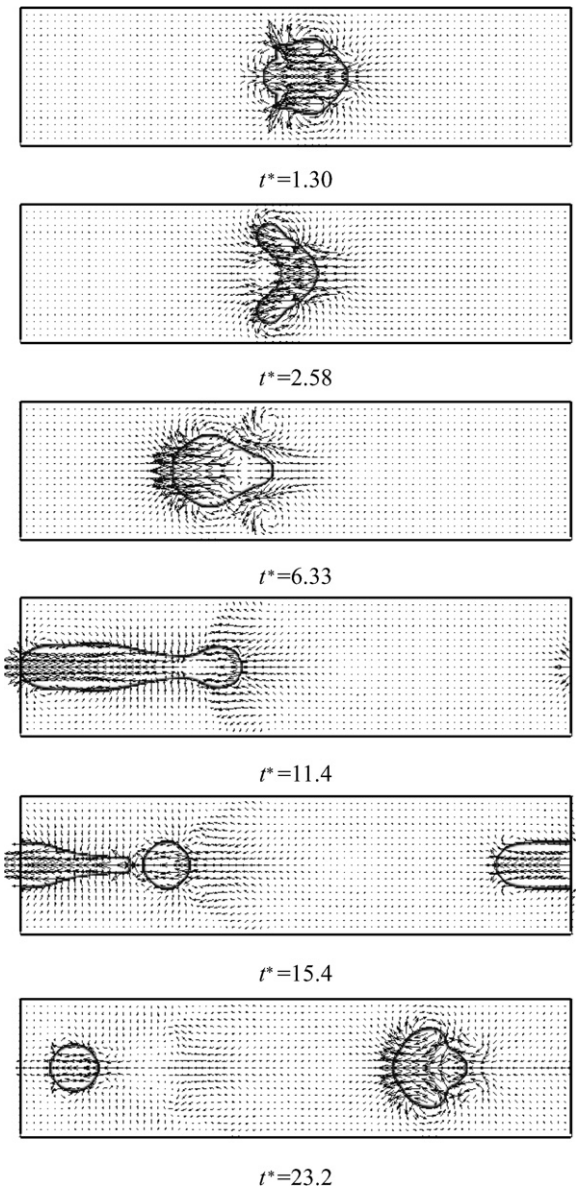


Fig. 4. Time evolution of velocity vectors and density contours at $y = L_y/2$ for $\lambda = 0.5$, $We = 51.3$ and $B = 0$ $[t^* = 2tV/(D_l + D_s)]$.

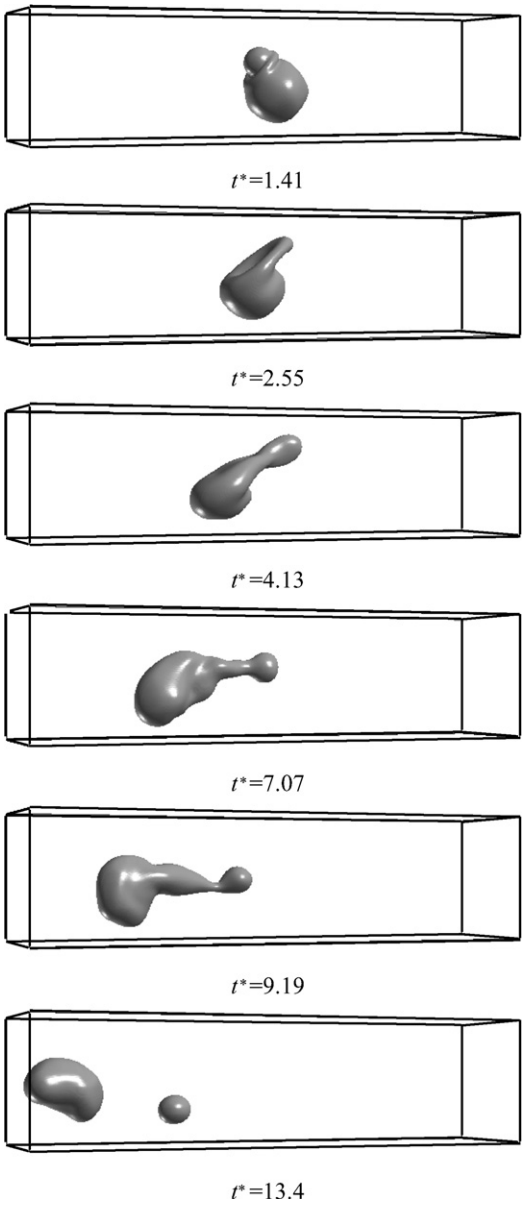


Fig. 5. Time evolution of droplet shape for $\lambda = 0.5$, $We = 61.5$, and $B = 0.6$ $[t^* = 2tV/(D_l + D_s)]$.

## 3. Results and discussion

Two liquid droplets with the diameters $D_l$ and $D_s$ are placed in a gas phase, and they collide with the relative velocity $V$ as shown in Fig. 1. Each droplet has the velocity $V/2$ in opposite directions with the distance $X$ which is measured from the center of one droplet to the relative velocity vector placed on the center of the other droplet (see Fig. 1). The density ratio of the liquid to the gas is $\rho_L/\rho_G = 50$ ($\rho_L = 50, \rho_G = 1$). The viscosities of the droplet and the gas are $\mu_L = 8.0 \times 10^{-2}\Delta x$ and $\mu_G = 1.6 \times 10^{-3}\Delta x$, respectively. The dimensionless parameters for binary droplet collisions are the diameter ratio $\lambda = D_s/D_l$, the Weber number $We = \rho_L D_s V^2/\sigma$, the Reynolds number $Re = \rho_L D_l V/\mu_L$, and the impact parameter $B = 2X/(D_l + D_s)$. The periodic boundary condition is used on all the sides of the domain. The half of the domain is calculated using the symmetry with $y = L_y/2$. The half domain is divided into a $640 \times 80 \times 160$ cubic lattice. The parameters in Eq. (9) are $a = 1, b = 6.7$, and $T = 3.5 \times 10^{-2}$; it follows that the maximum and minimum values of the order parameter are $\phi_{max} = 9.714 \times 10^{-2}$ and $\phi_{min} = 1.134 \times 10^{-2}$. The cut-off values of the order parameter are $\phi^*_L = 9.2 \times 10^{-2}$ and $\phi^*_G = 1.5 \times 10^{-2}$. The other parameters are fixed at $\kappa_f = 0.5(\Delta x)^2, \kappa_g = 3.0 \times 10^{-4}(\Delta x)^2, \tau_f = 1$, and $\tau_g = 1$. The relative velocity $V$ is changed in the range of $30 < We < 140$ and $3000 \leqslant Re \leqslant 4900$. In the following, two cases with the diameter ratios $\lambda = 0.5$ ($D_l = 80\Delta x, D_s = 40\Delta x$) and $\lambda = 0.25$ ($D_l = 80\Delta x, D_s = 20\Delta x$) are calculated.

### 3.1. Results for diameter ratio $\lambda = 0.5$

Fig. 2 shows the calculated results of time evolution of droplet shape for $We = 30.8$ and $B = 0.25$. The condition corresponds to $V = 0.85$ m/s, $D_l = 6.4$ mm and $D_s = 3.2$ mm in the collision of water droplets at 20 °C. The droplet shape represents the surface of $\rho = (\rho_L + \rho_G)/2$. After two droplets collide, they are formed into a disk-like droplet and then the coalescing droplet oscillates with forming various pear-shapes. The droplet never breaks in this case. This type of collision is called "coalescence collision". Fig. 3 shows the calculated results for $We = 51.3$ and $B = 0$. The time evolution of droplet shape is similar to the previous case up to $t^* = 6.33$. In this case, however, the droplet is formed into a long cylinder with rounded ends, and finally the cylinder breaks into two droplets. This type of collision is called "reflexive separation collision". The fluid velocity fields at $y = L_y/2$ are shown in Fig. 4. The complicated gas flows outside the droplets as well as liquid flows inside the droplets are clearly found. Fig. 5

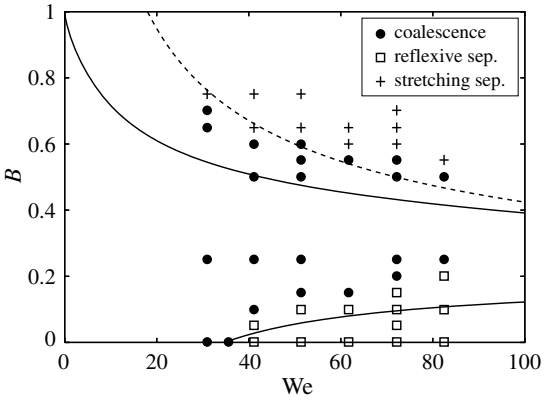


Fig. 6. Calculated results classified into three types of collisions for $\lambda = 0.5$. The solid curves represent the theoretical prediction of the boundaries between the three types of collisions by Ashgriz and Poo [2], and the broken curve represent the theoretical prediction of the boundary between the coalescence collision and the stretching separation collision by Brazier-Smith et al. [16].

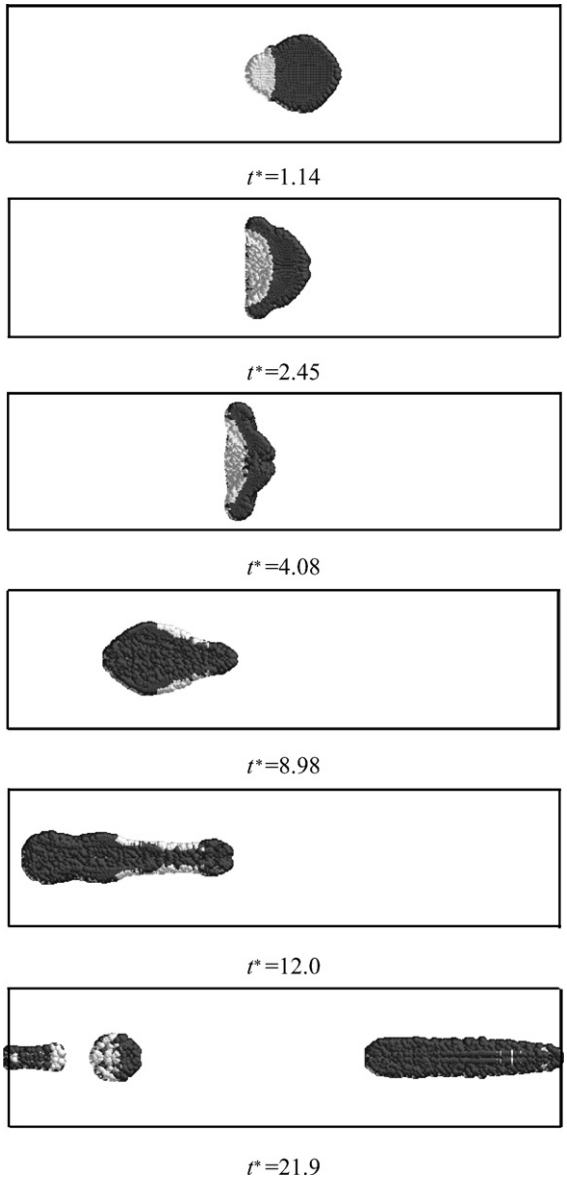


Fig. 7. Time evolution of tracer particles for $\lambda = 0.5$, $We = 78.8$, and $B = 0.19$ [$t^* = 2tV/(D_l + D_s)$]. The particles in $y \geqslant L_y/2$ are viewed from $y = -\infty$.

shows the calculated results for $We = 61.5$ and $B = 0.6$. Since the two droplets collide at the high impact parameter, only a portion of them contacts directly, and the remaining portions of the droplets tend to move in the direction of their initial velocities and consequently stretch the region of the interaction. Finally, the droplet breaks into two droplets. This type of collision is called "stretching separation collision".

We calculated for various Weber numbers and impact parameters, and classified the results into the above-mentioned three types of collision in the *We*–*B* plane as shown in Fig. 6. It is seen that the reflexive separation collisions appear in the region of low impact parameters and high Weber numbers over a critical value, and the stretching separation collisions occur at high impact parameters. The coalescence collisions occur between the two regions. In the figure, the theoretical predictions of the boundaries of the three types of collisions by using a simple energy balance analysis of Ashgriz and Poo [2] and Brazier-Smith et al. [16] are also drawn. The present calculated results are in good agreement with the theoretical prediction by Brazier-Smith et al. for the boundary between the coalescence and the stretching separation, although the boundary between the reflexive separation and the coalescence of the present results is shifted a little to the larger *B* from the theoretical prediction by Ashgriz and Poo.

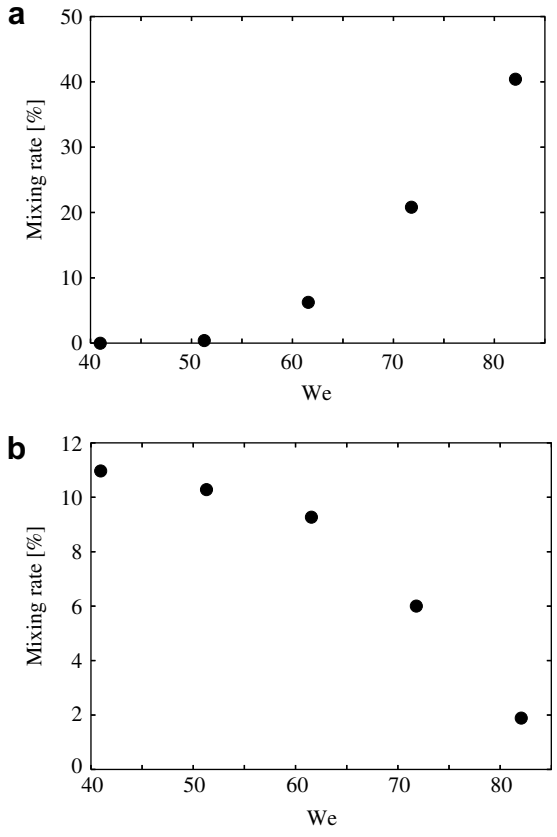


Fig. 8. Mixing rate versus *We* for $\lambda = 0.5$ and $B = 0$; (a) smaller droplet, (b) larger droplet.

The study of the mixing process during collisions is an important issue. By tracing fluid particles in two droplets, we investigate the mixing of fluids in two colliding droplets. The locations of the fluid particles at every time step are calculated by using the fourth-order Runge–Kutta method. Note that the particles going out of the droplets due to numerical errors are omitted in the calculation. Fig. 7 shows the calculated results for $We = 82.1$ and $B = 0$. In the figure the particles in $y \geqslant L_y/2$ are viewed from $y = -\infty$. Initially about 5300 white and 42,000 black particles are embedded in the small and the large droplets, respectively. After two droplets collide, the white particles penetrate to the black particles at $t^* = 2.45$ and 4.08, but after that the white particles move outside the black particles at $t^* = 8.98$ and 12.0. Finally, the droplet breaks into

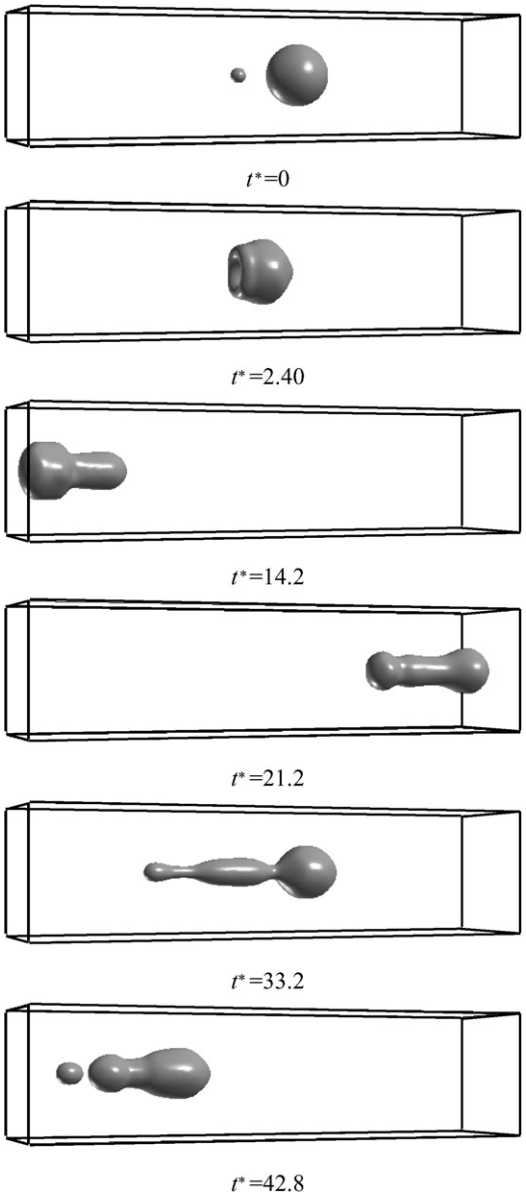


Fig. 9. Time evolution of droplet shape for $\lambda = 0.25$, $We = 89.6$, and $B = 0$ $[t^* = 2tV/(D_l + D_s)]$.

two partially mixed droplets. The mixing rate, which is defined here by the percentage of the number of the white particles in the total number of particles in the separated droplet, can be calculated by counting the number of the white and black particles in the separated droplet. At $t^* = 21.9$ in Fig. 7, the mixing rates obtained are 1.9% for the larger droplet and 40.4% for the smaller droplet. We calculated the mixing rate for various Weber numbers $We$ at $B = 0$, and the results are shown in Fig. 8. It is seen from Fig. 8 that as the Weber number increases, the mixing rate for the smaller droplet increases, while the mixing rate for the larger droplet decreases. That is, after the collision a larger portion of the small droplet moves to the other side through the outside of the large droplet, as the Weber number increases.

### 3.2. Results for diameter ratio $\lambda = 0.25$

Next, the results for $\lambda = 0.25$ are shown. Fig. 9 shows the calculated results of time evolution of droplet shape for $\lambda = 0.25$, $We = 89.6$ and $B = 0$. The condition corresponds to $V = 5.3$ m/s, $D_l = 0.94$ mm and $D_s = 0.23$ mm in the collision of water droplets at 20 °C. After two droplets collide, a hollow surface is formed in the coalescing droplet, and then the hollow repelled by the surface tension with forming into a long cylinder with two necks and rounded ends. Finally, the droplet breaks into two droplets at the front neck. In addition, we found that the coalescing droplet breaks into two droplets at the middle neck for $We = 99.6$ and it breaks into three droplets at the two necks for $We = 120$. These are all called "reflexive separation col-

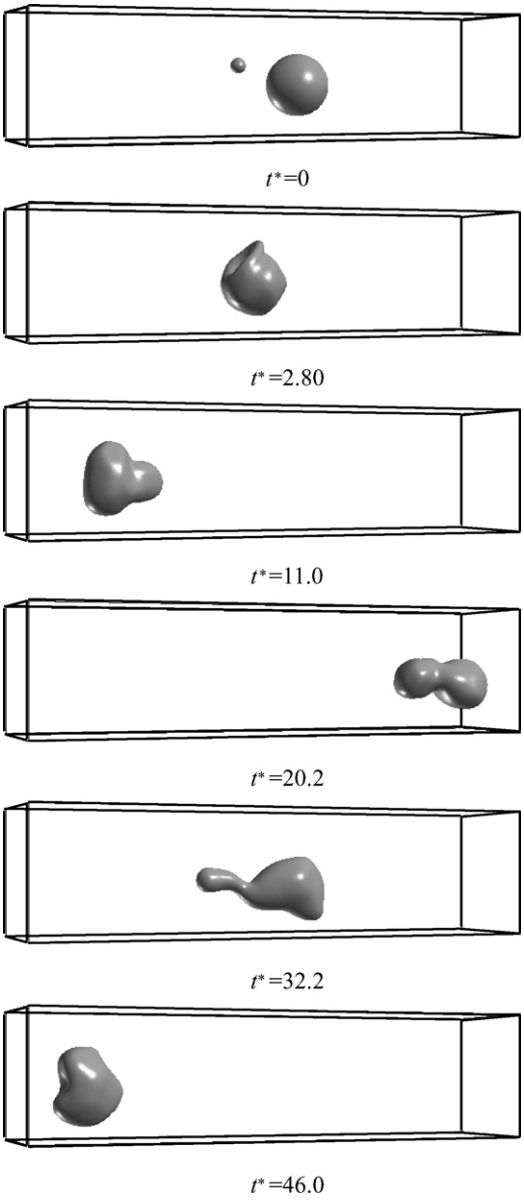


Fig. 10. Time evolution of droplet shape for $\lambda = 0.25$, $We = 89.6$, and $B = 0.5$ $[t^* = 2tV/(D_l + D_s)]$.

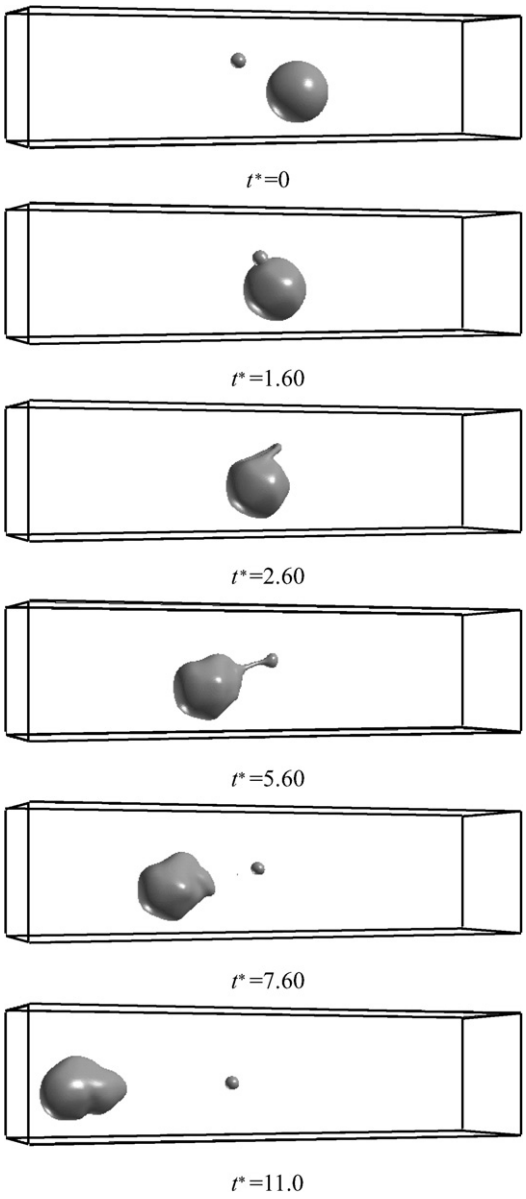


Fig. 11. Time evolution of droplet shape for $\lambda = 0.25$, $We = 89.6$, and $B = 0.8$ $[t^* = 2tV/(D_l + D_s)]$.

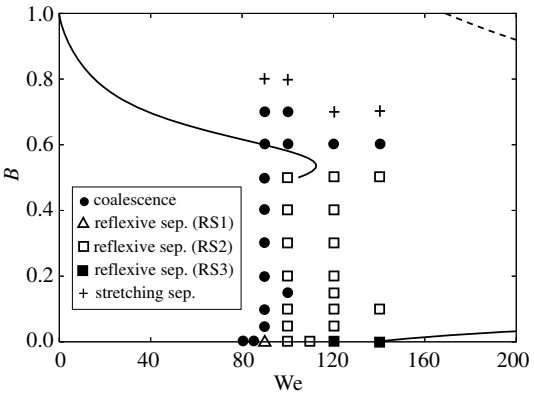


Fig. 12. Calculated results classified into three types of collisions for $\lambda = 0.25$. The solid curves represent the theoretical prediction of the boundaries between the three types of collisions by Ashgriz and Poo [2], and the broken curve represent the theoretical prediction of the boundary between the coalescence collision and the stretching separation collision by Brazier-Smith et al. [16].

lision", but hereafter we call the first case as RS1, the second case as RS2, and the third case as RS3. Next, Fig. 10 shows the calculated results of time evolution of droplet shape for $\lambda = 0.25$, $We = 89.6$ and $B = 0.5$. It is seen that the coalescing droplet is formed into complicated shapes, but it never breaks. The type of this collision is "coalescence collision". Fig. 11 shows the calculated results of time evolution of droplet shape for $\lambda = 0.25, We = 89.6$ and $B = 0.8$. This is clearly "stretching separation collision". It is noted that during the collision the larger droplet is formed into complicated shape, although the smaller droplet is little deformed. We calculated for various Weber numbers and impact parameters, and classified the calculated results into the three types of collision in the *We*–*B* plane as shown in Fig. 12. In this case, the theoretical predictions of the boundaries of the three types of collisions by Ashgriz and Poo [2] and Brazier-Smith et al. [16] do not work so well. It is found from Fig. 12 that the reflexive separation collisions occur in the wide range of $We > 90$ and $0 \leqslant B < 0.6$ where the theoretical predictions fail.

## 4. Concluding remarks

We have applied the lattice Boltzmann method for two-phase fluid flows with large density ratios to the simulations of collision dynamics of two unequal-size droplets for various Weber numbers and impact parameters. The calculated results are classified into three types of collisions, namely coalescence, reflexive separation, and stretching separation collisions, and are compared with the theoretical predictions. It is noted that the boundaries of the three types of collisions are obtained from the present results with the diameter ratios of $\lambda = 0.25$ where the theoretical predictions fail.

Also, we have investigated the feature of mixing processes during separating collisions by tracing colored particles embedded in the droplets. It is found from the results with the diameter ratios of $\lambda = 0.5$ that as the Weber number increases, the mixing rate for the smaller droplet increases, while the mixing rate for the larger droplet decreases.

In this paper, we do not deal with other types of binary droplet collisions such as a bouncing collision for low Weber numbers and a shattering collision for high Weber numbers. We are currently trying to simulate these types of collisions by the present method. In addition, the simulation for higher density ratios (e.g., 1000) is of importance in future work.

## Acknowledgements

This work is supported partly by the Grant-in-Aid for Scientific Research (No. 18360089) from JSPS and by the COE program (the Center of Excellence for Research and Education on Complex Functional Mechanical Systems) of the Ministry of Education, Culture, Sports, Science and Technology, Japan.

## References

[1] G. Brenn, A. Frohn, Collision and merging of two equal droplets of propanol, Exp. Fluids 7 (1989) 441–446.
[2] N. Ashgriz, J.Y. Poo, Coalescence and separation in binary collisions of liquid drops, J. Fluid Mech. 221 (1990) 183–204.
[3] M. Orme, Experiments on droplet collisions, bounce, coalescence and disruption, Prog. Energy Combust. Sci. 23 (1997) 65–79.
[4] J. Qian, C.K. Law, Regimes of coalescence and separation in droplet collision, J. Fluid Mech. 331 (1997) 59–80.
[5] M. Rieber, A. Frohn, Navier–Stokes simulation of droplet collision dynamics, in: Proceedings of 7th International Symposium on CFD, Beijing, China, 1997, pp. 520–525.
[6] F. Mashayek, N. Ashgriz, W.J. Minkowycz, B. Shotorban, Coalescence collision of liquid drops, Int. J. Heat Mass Transfer 46 (2003) 77–89.
[7] T. Inamuro, S. Tajima, F. Ogino, Lattice Boltzmann simulation of droplet collision dynamics, Int. J. Heat Mass Transfer 47 (2004) 4649–4657.
[8] M. Dai, D.P. Schmidt, Numerical simulation of head-on droplet collision: effect of viscosity on maximum deformation, Phys. Fluids 17 (2005) 041701.
[9] Y. Pan, K. Suga, Numerical simulation of binary liquid droplet collision, Phys. Fluids 17 (2005) 082105.
[10] K.N. Premnath, J. Abraham, Simulations of binary drop collisions with a multiple-relaxation-time lattice-Boltzmann model, Phys. Fluids 17 (2005) 122105.
[11] Y. Meleán, L.Di.G. Sigalotti, Coalescence of colliding van der Waals liquid drops, Int. J. Heat Mass Transfer 48 (2005) 4041–4061.
[12] M.R. Swift, W.R. Osborn, J.M. Yeomans, Lattice Boltzmann simulation of nonideal fluids, Phys. Rev. Lett. 75 (1995) 830–833.
[13] T. Inamuro, M. Yoshino, F. Ogino, Accuracy of the lattice Boltzmann method for small Knudsen number with finite Reynolds number, Phys. Fluids 9 (1997) 3535–3542.
[14] J.S. Rowlinson, B. Widom, Molecular Theory of Capillarity, Clarendon Press, Oxford, 1982, pp. 50–68.

[15] T. Inamuro, T. Ogata, S. Tajima, N. Konishi, A lattice Boltzmann method for incompressible two-phase flows with large density differences, J. Comput. Phys. 198 (2004) 628–644.
[16] P.R. Brazier-Smith, S.G. Jennings, J. Latham, The interaction of falling water drops: coalescence, Proc. Roy. Soc. Lond. A 326 (1972) 393–408.
[17] T. Inamuro, Lattice Boltzmann methods for viscous fluid flows and for two-phase fluid flows, Fluid Dynam. Res. 38 (2006) 641–659.
[18] Y. Sone, Molecular Gas Dynamics, Birkhäuser, Boston, 2007 (Chapter 4), pp. 73–167.